Surface & Coatings Technology xxx (xxxx) xxx–xxx

Contents lists available at ScienceDirect

Surface & Coatings Technology

journal homepage: www.elsevier.com/locate/surfcoat

Tunable ion flux density and its impact on AlN thin films deposited in a confocal DC magnetron sputtering system

M. Trant[a,*], M. Fischer[a], K. Thorwarth[a], S. Gauter[b], J. Patscheider[c,1], H.J. Hug[a,d]

[a] Empa, Swiss Federal Laboratories for Materials Science and Technology, Überlandstrasse 129, Dübendorf 8600, Switzerland
[b] Institute of Experimental and Applied Physics, Christian-Albrechts-University Kiel, Leibnizstr 19, Kiel D-24098, Germany
[c] Evatec AG, Hauptstrasse 1a, Trübbach CH-9477, Switzerland
[d] Department of Physics, University of Basel, Klingelbergstrasse 82, Basel 4056, Switzerland

ARTICLE INFO

Keywords:
Magnetron sputtering
Thin films
Aluminum nitride
Plasma
Ion bombardment
Magnetic configuration

ABSTRACT

An in-situ coil implemented in a confocal magnetron sputtering system is used to modify the ion flux impacting the substrate, thereby tuning the ion-to-neutral ratio. Plasma characterization performed at the substrate is used to map the spatial dependence of the ion flux density and the total energy flux density across the substrate holder. In addition, spatially-resolved temperature measurements are performed for different plasma conditions. Aluminum nitride (AlN) thin films were deposited by reactive sputtering in the fully poisoned mode on Si (100) and borosilicate glass substrates using the open field configuration. Texture, growth morphology, and residual stress of the films were determined and correlated with the plasma conditions and substrate temperatures obtained by applying the coil's magnetic field. All AlN films were stoichiometric and showed a hexagonal structure with (001) texture. The film stress was found to change from 0.9 GPa (tensile) to 4 GPa (compressive) with increasing ion flux density. Electron microscopy revealed an evolution from an open grain boundary to a dense film morphology compatible with the observed residual stress dependence of the films on the ion flux. No change in residual stress and film morphology was observed within the 100 °C–500 °C temperature range used here.

1. Introduction

In sputter deposition processes the ion impact on the growing film can be utilized advantageously to control the film microstructure and microchemistry [1-3]. For example, increasing the energy flux of the ions hitting the substrate, a compact film microstructure can be obtained already at a lower deposition temperature.

The ion bombardment processes are governed by the flux of incoming ions j_{ion} and their energy E_{ion}. The ion energy determines the mechanism of momentum transfer and the resulting effects [4]. In the case of low energy ion bombardment ($E_{ion} < 50$ eV) decremental effects of ion irradiation (e.g. creation of defects or vacancies, implantation) are avoided and the adatom mobility is enhanced collisionally. The latter results in an enhanced surface diffusion and rearrangement for atoms on the surface of the growing film. For a given E_{ion} the flux of incoming ions j_{ion} determines the total amount of energy transferred to the growing film.

It is crucial to control these two parameters independently, as their combination, the average energy per deposited atom, is not a universal parameter [5]. The ion flux and ion energy are also influenced by pressure and applied substrate bias. The pressure determines the mean free path of both the ions and neutral particles, and thereby influences the energy and flux of both species. The application of a bias controls the ion impact energy but may lead to implantation of the process gas, which leads to strain fields and lattice distortions [6].

The importance of controlling E_{ion} and j_{ion} directly and independently is widely recognized and a variety of approaches to control the plasma flux in deposition systems have been proposed and are still developed further [7]. Petrov et al. used a variable magnetic field generated by a pair of Helmholtz coils placed around the chamber of their single magnetron deposition system to directly control the flux of the ions impacting the sample [8]. Engström et al. adapted the use of a coil to a dual magnetron system designed for the deposition of thin film multilayers [9]. Here we present how this approach can be used for a multiple magnetron system that allows deposition of compound films from elemental targets. Within this work we also compare the open field to the closed field configuration of confocal magnetron sputtering as it was observed that the magnetic orientation of the magnetrons relative to each other has a strong influence on the plasma flux towards the substrate [10]. Confocal reactive sputtering is widely employed in

* Corresponding author.
E-mail address: mathis.trant@empa.ch (M. Trant).
[1] Empa, Swiss Federal Laboratories for Materials Science and Technology, Überlandstrasse 129, 8600 Dübendorf, Switzerland (until 31.10.2017).

https://doi.org/10.1016/j.surfcoat.2018.04.091
Received 4 December 2017; Received in revised form 26 April 2018; Accepted 28 April 2018

research and production for deposition of compound films from elemental targets. As an example we deposited aluminum nitride (AlN) thin films by reactive sputtering, which is the base material for many interesting compounds such as AlSiN for tribological or AlScN for piezoelectric applications [11,12].

AlN thin films have been studied extensively for applications in microelectronic, electroacoustic and optoelectronic devices [13-16]. In order to obtain good piezoelectric properties, polycrystalline wurtzite AlN films with a pronounced c-axis orientation must be achieved [16,13]. For their application in MEMS devices the preferred film properties need to be obtained at low deposition temperatures, and residual stress must be well controlled [17,18]. To achieve these properties appropriately adjusted ion flux and ion energy are advantageous.

2. Experimental setup

The experiments were performed on an AJA ATC 1500F sputtering system with 33 cm in height and a diameter of 37 cm, containing four magnetrons. Two of them were confocally inclined at an angle of 25° with respect to the z-axis and with the center of the targets separated by 15 cm, as schematically shown in Fig. 1, while the other two remained upright along the chamber walls. The magnetrons are unbalanced of type II [19] with an unbalancing factor of $K = \Phi_{mag}^{out}/\Phi_{mag}^{in} = 13$.

Elemental aluminum targets (99.999% purity) with a diameter of 5 cm were used, and the power supplies (Advanced Energy MDX 500) were operated in direct current constant power mode at 200 W and connected to a common ground. The heatable substrate holder, with a diameter of 89 mm, was oriented face down and its center located at a distance of 12 cm from the center of the targets.

Argon (6.0 purity) was used as a process gas and nitrogen (5.0 purity) was added for the case of reactive sputtering. Purifiers (Alphagaz O_2-free) were installed on both gas lines to further reduce the remaining oxygen concentration and moisture. The chamber is equipped with a turbomolecular pump (210 ls)and the base pressure of the chamber was better than 5×10^{-7} mbar.

A water-cooled coil was built and installed inside the vacuum chamber around the substrate holder. The coil consists of Kapton insulated copper wire with a core diameter of 1.7 mm. A total of 149 turns fit over a length of 58 mm and an inner and outer diameter of 176 mm and 244 mm respectively. The magnetic field of the coil ($\vec{B}_{coil}$) reaches 180 mT at the substrate holder surface for a coil current (I_{coil}) of 26 A. The magnetic field strength along the z-axis for $I_{coil} = 26$ A is included in the schematic of the setup shown in Fig. 1.

2.1. Plasma diagnostics

Several methods were employed to measure selected plasma parameters in the open field (OF) and closed field (CF) configurations, and for varying $\vec{B}_{coil}$ (see Fig. 1).

The substrate holder was used as an electrical probe to measure the floating potential (V_{float}) and the ion saturation current (I_{sat}). For the latter, a bias of $V_{bias} = -60$ V was applied to the substrate holder.

A commercial Langmuir probe (LP) acquisition system (ALP, Impedans LTD) was used to acquire current-voltage data (I–V data). A cylindrical tungsten wire, with a diameter $r_{LP} = 50$ µm and a length $l_{LP} = 10$ mm, was used as a probe tip. The probe was installed on a linear positioner to measure the ion current density (j_p), the plasma potential (V_p) and V_{float} as a function of the x-position (see Fig. 1).

An active thermal probe (ATP) was alternatively installed onto the same positioner to measure the total energy flux to the substrate. The ATP consist of a Pt100 resistor embedded in an insulating ceramic 7 mm wide and 10 mm long [20].

The LP and ATP were positioned about 13 mm below the substrate holder. The measurements mentioned above were conducted in a pure Ar atmosphere to avoid the problem arising from the formation of an insulating layer on the probes' surfaces. The Ar flow was set to 15 sccm and the pumping speed was adjusted to obtain a working pressure of approximately 5 µbar.

2.2. Depositions

AlN thin films were deposited onto Si (100) and borosilicate glass substrates, both $6 \times 6\,mm^2$, using the open field configuration. The samples were mounted close to the center (position x_i in Fig. 1), at a middle radius (x_m) and at the outer rim (x_o) of the substrate holder. Note that the substrate holder was not rotated during the deposition process. Prior to the deposition process, the substrates were ultrasonically cleaned for 10 minutes in a mixture of acetone and ethanol.

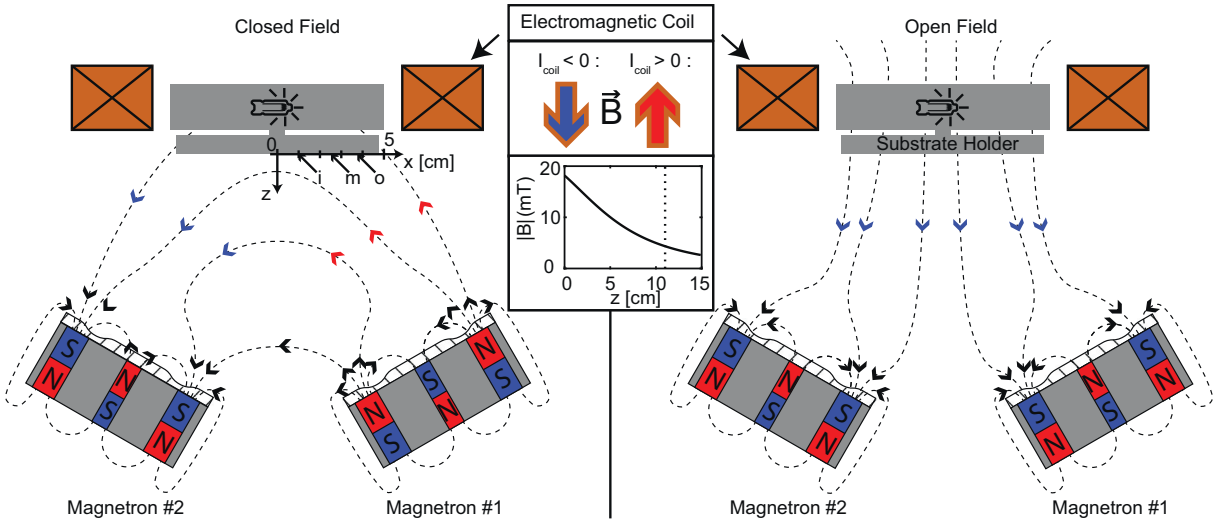

Fig. 1. Schematics of the experimental setup showing the closed field (left side) and open field (right side) configuration with a qualitative representation of the magnetic field lines arising from the magnetrons ($I_{coil} = 0$ A). The substrates were placed at three different positions along the x-axis ($x_i = 1$ cm, $x_m = 2.5$ cm, $x_o = 3.75$ cm). By inverting the current inside the electromagnetic coil the direction of the magnetic field can be reversed. The graph shows the magnetic field strength as a function of the vertical position along the central axis of the coil for $|I_{coil}| = 26$ A. Position $z = 0$ corresponds to the substrate holder surface position and the dotted line indicates the z-position of the target. (For interpretation of the references to color in this figure, the reader is referred to the web version of this article.)

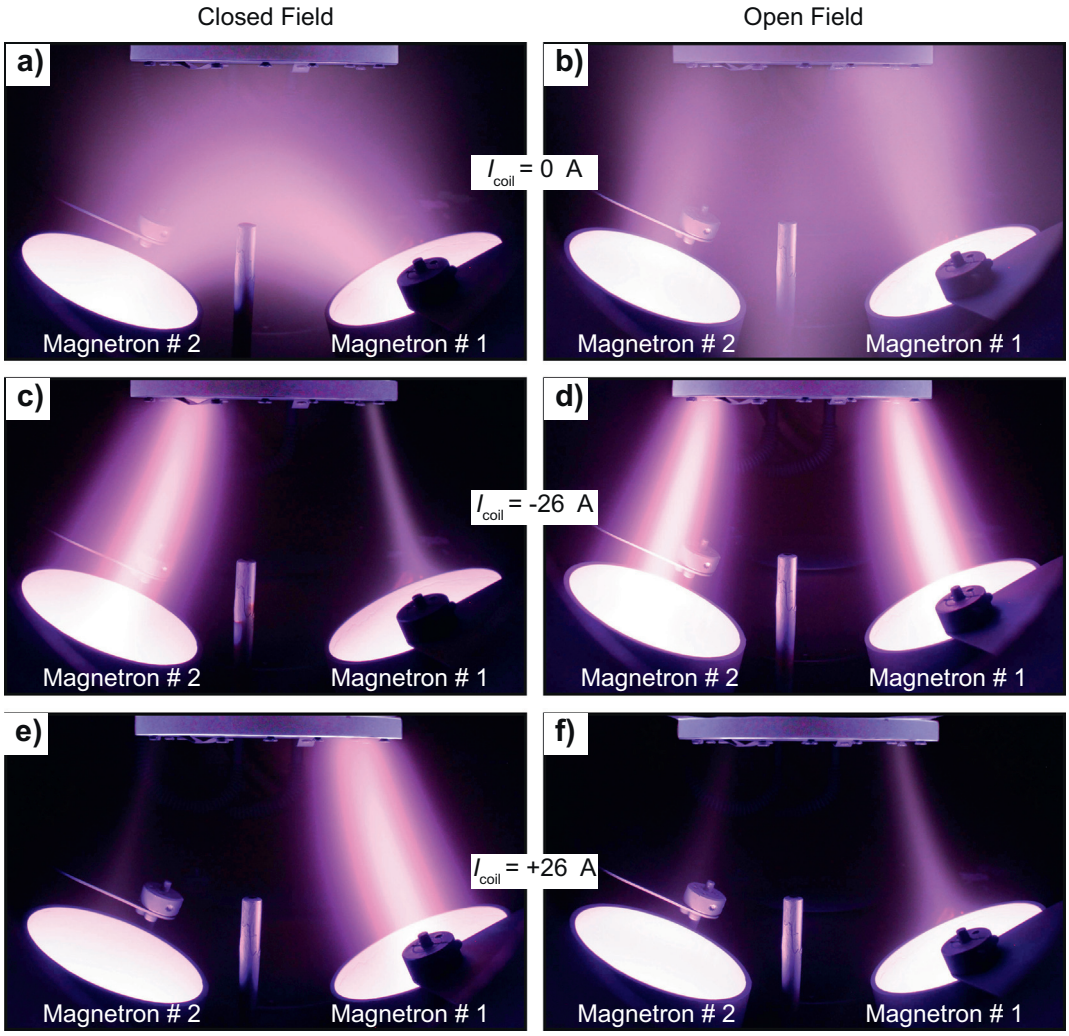

Fig. 2. Photographs of the plasma for different magnetron configurations and coil currents I_{coil}. The magnetrons were operated in a pure Argon atmosphere with conditions as described in Section 2.2. The photographs were taken with fixed aperture, shutter speed and ISO setting for comparability.

After transfer to the process chamber the samples were plasma cleaned by applying a 13.56 MHz RF bias of − 75 V to the substrate holder for 2 minutes in an argon atmosphere. This was followed by a target cleaning step (3 minutes), to initially bring the target into its metallic state, and a target poisoning step (2 minutes), both performed with closed magnetron shutters. Depositions were carried out in the fully poisoned state with a flow of $\phi = \phi_{Ar} + \phi_{N2} = 15$ sccm + 12 sccm, and the pumping speed was adjusted to obtain a pressure of approximately 5 μbar.

To determine the working point in the fully poisoned state, a hysteresis curve was recorded and a nitrogen flow rate in the reactive mode well beyond the transition region was chosen.

The deposition time was kept constant at 120 minutes, and the substrate holder was left at floating potential. After deposition the target was again brought into its metallic state by an additional target cleaning step (3 minutes).

I–V data were also recorded at $t = 30$ min and $t = 90$ min during film deposition at the positions x_i, x_m and x_o with a Langmuir probe length $l_{LP} = 5$ mm, smaller than the width of the substrates (6 mm). One LP data acquisition cycle was performed within less than a minute. For the rest of the process the probe was retracted from the deposition chamber. Before each data acquisition cycle the probe was cleaned by application of a positive bias of 100 V, leading to electron bombardment and consecutive heating of the probe.

The deposition system is equipped with a substrate heater to vary the temperature of the substrates during film growth. The temperature of the latter can, however, become considerably higher, if the plasma conditions lead to an additional energy influx to the sample surface. To calibrate the substrate surface temperature we used silicon wafer pieces with type K thermocouples attached to the surface facing the plasma. The thermocouples were attached with an electrically insulating and thermally conducting ceramic glue (Omega CC). Temperature measurements were performed at the locations x_i, x_m and x_o.

2.3. Thin film characterization techniques

The film thickness was measured with a stylus profiler (DektakXT, Bruker). The residual stress of the thin films was determined for the borosilicate glass samples using the Stoney equation and the radius of curvature, measured with a confocal microscope (DCM8, Leica) [21].

Atomic composition was determined by Rutherford Backscattering (RBS) with 2 MeV He for the Si substrates. Additionally, elastic recoil detection analysis (ERDA) with 13 MeV ^{127}I was used to refine the oxygen concentration. More details about the RBS and ERDA analysis are described elsewhere [22]. The crystalline texture was analyzed for the Si substrates by X-ray diffraction (XRD), set up in a symmetric $2\theta - \theta$ geometry with a parallel beam, using Cu Kα radiation (D8, Bruker). A nickel filter was used to eliminate the Cu Kβ radiation.

SEM micrographs of the film cross sections were taken for the Si substrates to analyze the growth morphology. The SEM (Hitachi, S-

4800) was operated at 1 keV and a magnification of 60×10^3.

3. Results and discussion

3.1. Plasma characterization

The CF and OF setup are displayed in Fig. 1. For the CF case the arrangements of the magnets of magnetrons #1 and #2 are antisymmetric to each other, leading to closed field lines between the magnetrons. For the symmetric OF case the magnets of both magnetrons have the same orientation. This results in parallel magnetic field lines in the region between the magnetrons and the substrate holder (called far field region in the following). In our specific setup the far field of magnetron #2 is parallel to the field generated by the coil for negative currents for the OF and CF configuration. For magnetron #1 this is true for the OF configuration only, since its magnets are reversed in the CF configuration and its far field then becomes anti-parallel to $\overrightarrow{B_{\text{coil}}}$ for $I_{\text{coil}} < 0$ (colored arrows).

Fig. 2 displays photographs of the plasma for different operating conditions. Panels a) and b) show the plasma without an additional applied field for the CF and OF configuration, respectively. The bright areas indicate regions of high plasma density, and their geometry resembles that of the field lines (Fig. 1). Panels c), d), e) and f) show the plasma in an applied field. For $I_{\text{coil}} = -26$ A the applied field is parallel to the far field of magnetron #2 for the CF configuration, and parallel to both magnetrons for the OF configuration (Fig. 1). The plasma then extends from the magnetron(s) to the substrate. In the closed field configuration the plasma of magnetron #1 remains localized at the magnetron. For $I_{\text{coil}} = +26$ A the applied field is now parallel only to the far field of magnetron #1 for the CF configuration.

3.1.1. Ion saturation current and floating potential measured with the substrate holder

For magnetron sputtering the floating potential (V_{float}) of the substrate and the ion saturation current (I_{sat}) flowing into the substrate are often used for plasma characterization.

The floating potential is related to the plasma potential (V_{p}) as

$$V_{\text{float}} = V_{\text{p}} + \frac{k_{\text{B}} T_{\text{e}}}{e} \ln\left[0.61\sqrt{2\pi\frac{m_{\text{e}}}{m_{\text{i}}}}\right], \tag{1}$$

where T_{e} is the electron temperature, k_{B} is the Boltzmann constant, e is the elementary charge, and m_{i} and m_{e} are the ion and electron mass, respectively.

The ion saturation current is given by

$$I_{\text{sat}} = 0.61 \int_{A_{\text{probe}}} e n_{\text{i0}} \sqrt{\frac{k_{\text{B}} T_{\text{e}}}{m_{\text{i}}}}\, dA \tag{2}$$

where n_{i0} is the ion density of the plasma (without mutual perturbations arising from the presence of the measurement probe), and the integral is carried out over the entire probe area (A_{probe}) [23].

In this study, we use these quantities to characterize the dependence of the plasma state on the coil current in the closed field and open field configuration, and for single and dual magnetron operation.

Fig. 3 displays the measurement results for the floating potential and the ion saturation current as a function of coil current. Data was taken for single and dual magnetron operation, and in OF and CF configuration. Both, V_{float} and I_{sat}, were measured with the substrate holder as an electrical probe.

First we discuss the results obtained for the operation of a single magnetron (#2, Fig. 1). For increasing negative coil currents, V_{float} saturates at approximately -18 V. For positive coil currents, V_{float} becomes less negative and rises to about -7 V. The additional magnetic field generated by the coil does not significantly affect the discharge current and voltage of the magnetrons. Therefore the electron temperature, which is given by the local plasma conditions at the magnetron, remains unaffected, and we conclude from Eq. (1) that V_{p} drops together with V_{float} for increasing coil currents.

The ion saturation current remains small for positive coil currents (c)), in agreement with the visual appearance of the plasma at magnetron #2 for positive coil currents (Fig. 2 e), f)). For increasing negative coil currents I_{sat} rises and then saturates at about 25 mA. The difference between the OF and CF setup is minute, indicating that $\overrightarrow{B_{\text{coil}}}$ dominates the fields arising from the interactions of the magnetrons in both configurations.

Panels b) and d) of Fig. 3 show the results for dual magnetron operation. The dependence of V_{float} on I_{coil} for the OF configuration is the same as that obtained during single magnetron operation (a), open symbols). The same is observed for the CF configuration for negative coil currents. However, for positive coil currents V_{float} is dominated by magnetron #1 with its far field then parallel to that of the coil. Consequently the dependence of V_{float} is symmetric with respect to the current direction. The symmetric behavior of the CF configuration is also observed for the ion saturation current (d), filled circles). In the OF configuration I_{sat} is doubled in every point compared to the single magnetron operation (c), open symbols). This increased current becomes apparent from Fig. 2 d) showing the extension of the plasma of each magnetron at the substrate holder, and Eq. (2) relating the ion saturation current to an integration over the substrate holder area.

The results demonstrate that with the field generated by the coil, I_{sat} can be varied by more than one order of magnitude. The consequences for the film growth will be discussed in Section 3.2. However, panels b) and d) in Fig. 2 show that the plasma density depends on the position on the substrate holder, which prevents a homogeneous deposition over a wide area of the substrate holder. At the same time, it provides us with the opportunity to deposit samples simultaneously under different plasma conditions. With our position-dependent measurement of the plasma conditions a correlation of plasma parameters and films properties becomes possible.

3.1.2. Ion and energy flux distributions

The photographs of the plasma shown in Fig. 2 suggest that the spatial distribution of the ion current density, and with it the energy flux provided by the plasma, is localized near the outer rim of the substrate holder ($\pm x_{\text{o}}$) for $I_{\text{coil}} = -26$ A.

The ion current density distribution and the total energy flux density for $x > 0$ (above magnetron #1), while powering both magnetrons in the closed field configuration, are shown in Fig. 4 a). As expected both show nearly Gaussian distributions with centers on the outer part of the substrate holder and almost identical widths. The small differences of the center position of the two distributions is believed to arise from the limited precision of the linear positioner and from the size of the probes. For $I_{\text{coil}} = 15$ A, the ion current density is reduced to about half of that obtained at $I_{\text{coil}} = 26$ A, and the centers position is shifted slightly towards the center of the substrate holder. For negative coil currents the ion current density becomes smaller than 2 mA m^{-2}.

The dependence of the ion current density on the coil current at position $x = 3$ cm is displayed in Fig. 4 b). For $I_{\text{coil}} > 0$ the ion current density increases rapidly, whereas it remains small for negative I_{coil}. This is consistent with the results of the ion saturation current data shown in Fig. 3 c). Note that the Langmuir and thermal probe measurements are performed above magnetron #1, whereas the ion saturation current measurements shown in Fig. 3 c) were performed operating magnetron #2 that has the opposite polarity than magnetron #1 for the closed field configuration. For this reason the dependence on the direction of the coil current is reversed.

The partial energy flux density from ions impacting on the electrically floating substrate (J_{ions} in W m^{-2}) is given by

$$J_{\text{ion}} = E_{\text{ion}} \cdot j_{\text{ion}}, \tag{3}$$

where j_{ion} is the ion flux in s^{-1} m^{-2} and $E_{\text{ion}} = e \cdot (V_{\text{p}} - V_{\text{float}})$ the ion

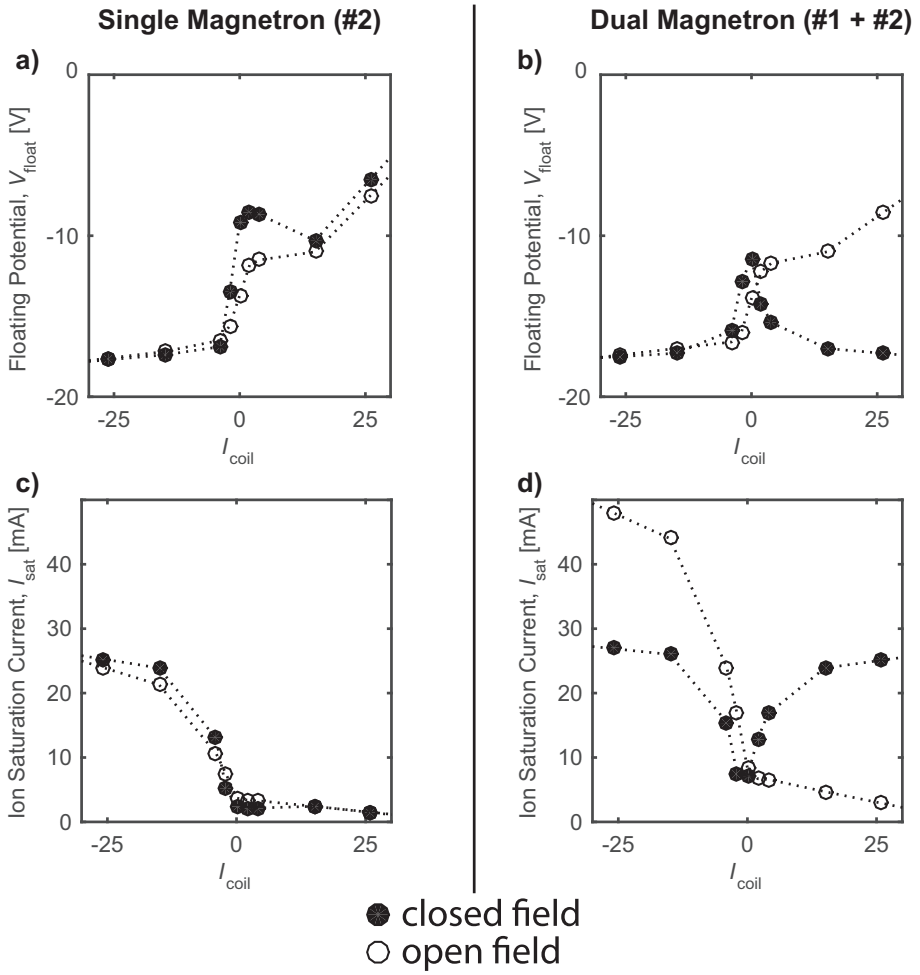

Fig. 3. Ion saturation current and floating potential as a function of the current in the coil for open field and closed field configuration. Here, the substrate holder was used as an electrical probe. Graphs a) and c) show the results of measurements performed powering a single magnetron. Note that in both cases magnetron #2 was used, which has the same magnetic arrangement for both configurations. Graphs b) and d) show the results of measurements where both magnetrons were powered simultaneously.

energy [24]. With the measured ion current density $j_p = j_{ion} \cdot e$ Eq. (3) becomes

$$J_{\text{ion}} = j_p\,(V_{\text{p}} - V_{\text{float}}), \tag{4}$$

where V_{p} and V_{float} are the measured plasma and floating potentials. We find that the ratio of J_{ion} to the total energy flux density (J_{tot} in W m^{-2}) is smaller than 0.1 for all data points. Hence, we conclude that most of the energy flux arises from electrons, radiation, and neutral atoms hitting the substrate [25].

3.2. Dependence of film properties on plasma parameters and temperature

The maximum achieved ion saturation current measured over the entire substrate holder is two times higher for the open field configuration than for the closed field configuration (see Fig. 3 d)). For applications where a high sample throughput or the use of different target materials requires a rotation of the substrate holder the open field configuration is more attractive, and we therefore choose this configuration for the depositions.

Aluminum nitride thin films were grown by reactive sputtering in the open field configuration with two magnetrons, each operated at 200 W constant power. All depositions lasted 120 min, and the substrate holder was left floating. The samples were clamped onto the substrate holder, which results in a rather high thermal resistance between them. The actual sample temperature can thus be different from that of the substrate holder. Therefore the sample temperatures arising from the sputter process were determined for all sample position and conditions in separate sputtering experiments. The ion current densities were measured at $t = 30$ min and $t = 90$ min during the thin film deposition by moving the Langmuir probe to the corresponding positions. Measuring at all three positions consecutively took less than 1 minute. Further details on the deposition conditions, Langmuir and temperature measurements are described in Section 2.2.

Table 1 shows the temperatures and ion current densities obtained at the three sample positions for the different deposition conditions. With the heater turned off, a sample temperature of 259 ° C was found at the position x_o for $I_{coil} = -24$ A, where the highest ion current density of 74 A m − 2 was obtained. A significant increase of the sample temperature to 349 ° C was also observed at x_o, with a substrate heater setpoint of 250 ° C.

The ion current densities vary about a factor of two across the substrate holder for $I_{coil} = 0$ A. For larger coil currents a substantial spatial variation of the temperatures and ion current densities across the substrate holder is observed. Those observations are compatible with the visual appearance of the plasma depicted in Fig. 2 b) and d).

We found that the dependence of the total energy flux and ion current density on the x-position is comparable to that measured for the closed field configuration (Fig. 4 a)), but that the position and the value of the maximum ion current density is slightly different. The position x_o matches with the maximum of the ion current density distribution of

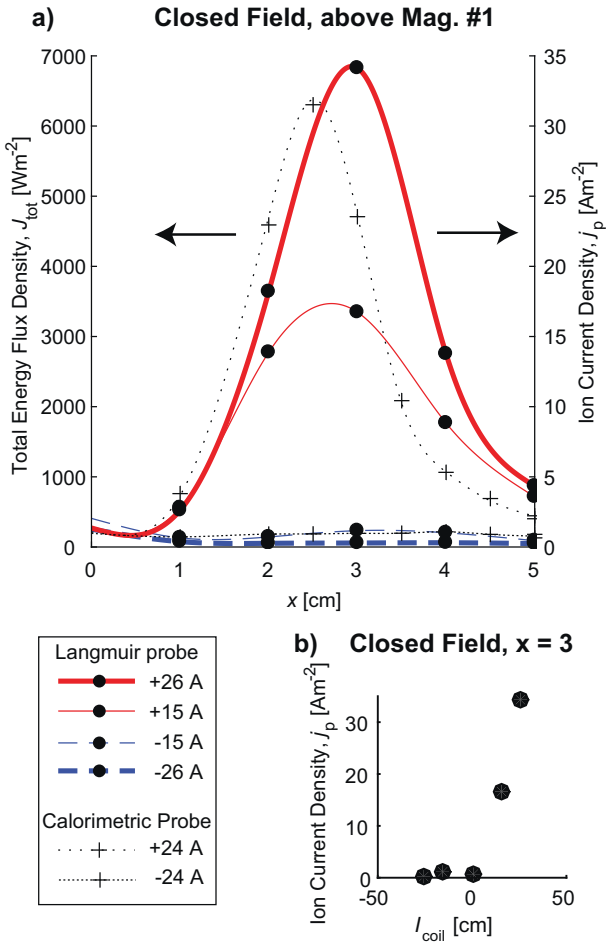

Fig. 4. Panel a) shows the total energy flux density (crosses, left axis) and ion current density (bullets, right axis) as a function of the x-position in the closed field configuration for various coil currents. The measurements were performed above magnetron #1 with the calorimetric and Langmuir probe. Panel b) shows the ion current density as a function of the coil current at position $x = 3$.

the open field configuration.

The film thicknesses were all in the range of 770 ± 100 nm, with a correlation between increasing film thickness and target consumption (race track depth). No dependence on the substrate temperature or on the ion current density was observed. From the latter we conclude that the applied magnetic field changes the ion to neutral ratio, while the flux of film-forming atoms to the substrate remains constant.

All films showed a stoichiometric AlN composition with a metal to non-metal ratio of 1:1. The oxygen content was below 2 at%. The argon concentration was found to be smaller than 0.07 at% for all films, independent of the ion flux density.

To analyze the dependence of the film properties on the different conditions observed at the sample positions x_i, x_m and x_o, the residual stress σ and XRD-diffractograms were measured for all samples, and the cross sections of selected samples were inspected.

Fig. 5 a) displays the dependence of the residual stress on the sample temperature for the position x_i (open circles), x_m (open squares), and x_o (open stars), respectively, without an external field ($I_{coil} = 0$). The residual stress of the films was found to depend on the ion current density, but not on the substrate temperature: The residual stress changes from 0.7 GPa (tensile) to −0.3 GPa, and −1.8 GPa (compressive) with the ion current densities of 2.5 A m^{-2}, 3.9 A m^{-2} and 5.5 A m^{-2} for the positions x_i, x_m and x_o respectively. The fact that the stress is independent of the sample temperature (for the temperature range covered here) can be attributed to the low homologous temperature. The

Table 1
Sample temperature (T) and ion current density (j_p) at the sample positions x_i, x_m and x_o for different experimental conditions. The letters in parentheses indicate the corresponding samples presented in Fig. 7.

Heater Setpoint	I_{coil} [A]	Position	T [°C]	j_p [A m^{-2}]
Heater Off	0	x_i (a)	108	2.4
		x_m	108	4
		x_o	108	5.9
	−12	x_i	141	2.7
		x_m	165	6.3
		x_o	245	56
	−24	x_i (d)	145	1.5
		x_m (e)	171	6.4
		x_o (f)	259	74
140°C	0	x_i	187	2.5
		x_m	187	4
		x_o	187	5.7
250°C	0	x_i (b)	250	2.5
		x_m	250	4.0
		x_o	250	5.7
	−12	x_i	–	–
		x_m	–	–
		x_o	–	–
	−24	x_i	275	2.6
		x_m	312	6.3
		x_o	349	72
500°C	0	x_i (b)	500	2.3
		x_m	500	3.7
		x_o	500	5.2

latter is defined as the deposition temperature normalized by the melting temperature of the deposited film material, and is smaller than 0.3 for all deposition temperatures used here.

Fig. 5 b) depicts the dependence of the residual stress σ on the ion current density j_p for all deposited samples. The residual stress changes linearly from 0.9 GPa (tensile) to −1.93 GPa (compressive) for $0 \le j_p \le 7$ A m^{-2} with

$$\sigma(j_p) = a \cdot j_p + b \ . \tag{5}$$

and

$$\begin{aligned} a &= (-0.47 \pm 0.13)\ \text{GPa m}^2\ \text{A}^{-1} \\ b &= (+1.56 \pm 0.6)\ \text{GPa}. \end{aligned} \tag{6}$$

For larger ion current densities, 7 A m^{-2} ≤ j_p ≤ 75A m^{-2}, the compressive residual stress increases at a lower rate to about −4 GPa with

$$\begin{aligned} a &= (-0.03 \pm 0.15)\ \text{GPa m}^2\ \text{A}^{-1} \\ b &= (-1.49 \pm 9.9)\ \text{GPa}. \end{aligned} \tag{7}$$

The dashed lines show the linear fits to the data points.

The dependence of the residual stress and the ion energy on the ion current density appear to be correlated (see Fig. 5 b) and c)). The ion energy was calculated as for Eq. (4) and increases linearly from 10 eV to 18 eV for $0 \le j_p \le 7$ A m^{-2} with

$$E_{ion}(j_p) = c \cdot j_p + d \quad . \tag{8}$$

and

$$\begin{aligned} c &= (+1.6 \pm 0.3)\ \text{eV m}^2\ \text{A}^{-1} \\ d &= (+6.8 \pm 1.3)\ \text{eV}. \end{aligned} \tag{9}$$

For ion current densities above 7 A m^{-2} it reaches a saturation at 22 eV. The intersection between the dashed lines indicate a change of slope at an ion current density of 10 A m^{-2}, close to that observed for the dependence of the residual stress on ion current density. This suggests that the steep decrease in residual stress for $0 \le j_p \le 7$ A m^{-2} can be attributed to an increase in both, the ion energy and the number of impacting ions (corresponding to an increasing ion current density). For higher ion current densities only the number of impacting ions changes and the decrease in residual stress becomes less steep.

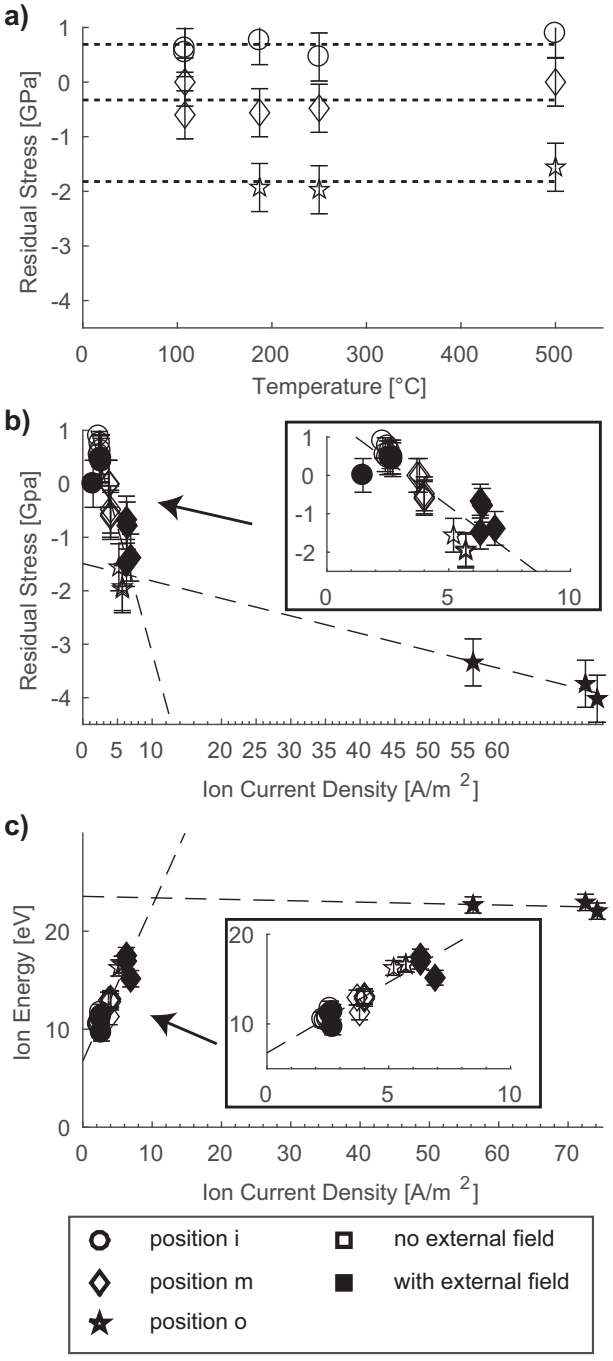

Fig. 5. Dependence of the residual stress on temperature (a) and ion current density (b). Graph c) shows the dependence of the ion energy ($E_{ion} = V_p - V_f$) on the ion current density. The dashed lines are linear fits to selected data points.

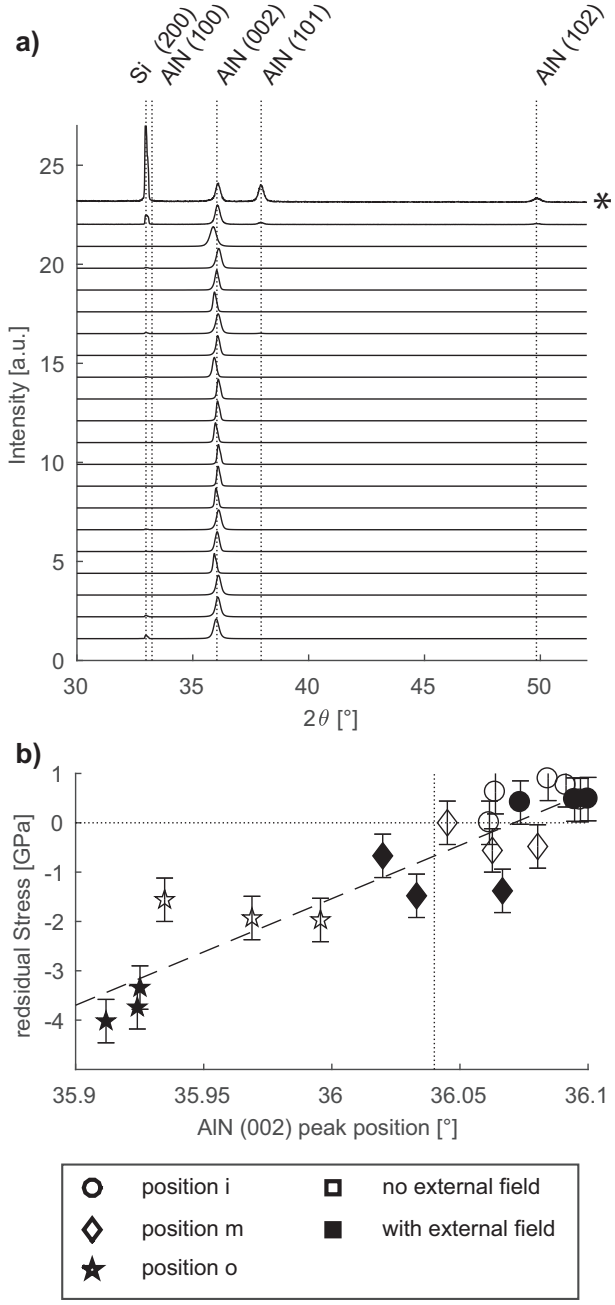

Fig. 6. Panel a) shows normalized XRD spectra of samples deposited under the conditions listed in Table 1 and are presented in the same order as therein. The sample at position x_i (position of lowest energy influx) deposited with the heater and the coil switched off (see Table 1) is marked by the *. The dotted lines indicate the peak position of Si and hexagonal wurtzite [33,34]. Panel b) shows the residual stress measured on the borosilicate glass samples plotted versus the AlN (002) peak position obtained from the $2\theta - \theta$ scans of the silicon samples. The dashed line shows the linear fit to the data, and the dotted lines indicate 0 residual stress and the AlN (002) peak position from literature respectively.

Our observations regarding the residual stress are in accordance with results from other groups. A change from tensile to compressive stress is commonly observed with increasing bombardment by energetic particles (neutrals or ions) for sputtered thin films [10,17]. This behavior is also found for the case of AlN depositions when the pressure, bias potential or the N2/Ar ratio is varied in order to change the bombardment of the growing film [17, 18, 26, 27]. However, variation of the before mentioned parameters might entail changes in other process parameters (i.e. IV-characteristics) or film composition (i.e. argon incorporation), which can be excluded in our work.

To study the crystallinity of the films XRD measurements were performed. The $2\theta - \theta$ scans, shown in Fig. 6 a), revealed that all films exhibit only the hexagonal wurtzite structure. In combination with rocking curves it was found that the c-axis is oriented perpendicular to the sample surface, except for the sample at position x_i (position of lowest energy influx, marked by the * in Fig. 6 a)) deposited with the heater and the coil switched off (see Table 1). This specific sample shows several XRD peaks of considerable intensity in the $2\theta - \theta$ scan which can be attributed to other planes of the AlN wurtzite phase,

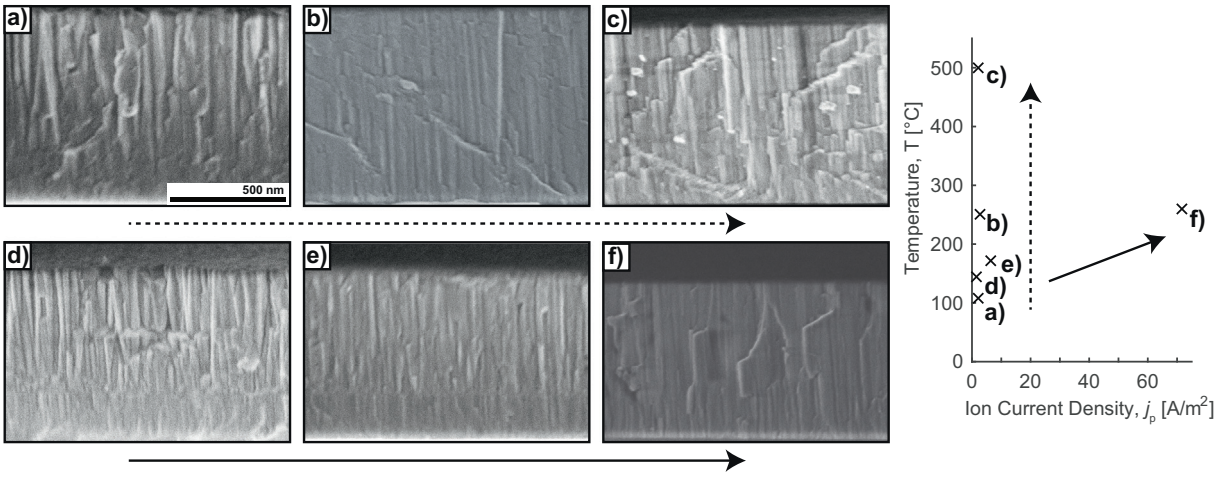

Fig. 7. Cross section morphology of selected samples imaged by SEM. Samples a), b) and c) were exposed to almost identical ion current densities but deposited at different temperatures. For the images d)–f) the ion current density increases, which is accompanied by a change in the substrate temperature because of the plasma heating. The values corresponding to the different deposition conditions are plotted in the graph on the right side, and are also listed in Table 1.

indicating that the preferential (001) orientation is lost. A pole figure analysis of a selected sample (sample f) in Fig. 7) showed the fibre texture typical for polycrystalline AlN. The (002) texture is commonly observed in literature for AlN thin films deposited by magnetron sputtering [28-31]. For a detailed discussion about the influence of the growth conditions on the texture we refer to previous work [32].

Fig. 6 b) shows the residual stress measured on the borosilicate glass samples plotted versus the AlN (002) peak position obtained from the $2\theta - \theta$ scans of the silicon samples. An in plane compressive stress of a thin film leads to a shift towards lower angles of the peak position, which is reflected by the negative slope of the data-fit (dashed line). The data-fit crosses the 0 residual stress line almost at the position of the literature value for the AlN (002) peak (dotted vertical line) confirming the good agreement of the data obtained by the different techniques and on different substrates.

Fig. 7 shows film cross sections of selected samples, where different growth morphologies can be observed. Panels a) to c) show samples grown at different temperatures and low ion current densities (< 2.5A m^{-2}). They exhibit well-oriented elongated crystalline grains with pronounced grain boundary contrast. This morphology is compatible with open grain boundaries leading to tensile film stress observed at low ion current densities (see Fig. 5 b)). The growth morphology is not affected by the temperatures used within this study, which is compatible with the residual stress that was also found to remain constant for these conditions. Panels d) to f) show the evolution of the morphology with increasing ion current density. At an ion current density of 1.5 A m^{-2} a film morphology similar to those visible in panels a) to c) is observed. For higher ion current densities (e) and f)) a vanishing grain boundary contrast is observed. This indicates an increase of the film density, and is compatible with the observed transition from tensile to compressive film stress with increasing ion current densities (Fig. 5 b)). Because the growth morphology did not change at increased temperatures, the observed densification at higher ion flux can be solely attributed to the change in ion bombardment. The above presented observations are in agreement with the extended structure zone diagram proposed by André Anders [1]. The observed transitions in the stress state and growth morphology are compatible with the transition from zone 1 to zone T with the pathway along the normalized energy axis.

4. Conclusion

An in-situ coil installed in a confocal magnetron sputtering system was used to tune the ion-to-neutral ratio by a factor of 30. Our present experimental setup did, however, not permit a homogeneous ion flux over the whole area of the substrate holder. Yet, for an experimental deposition system this inhomogeneity can be advantageous, because it allows the simultaneous deposition of samples exposed to different plasma conditions, and hence a study of the film properties on the plasma parameters, in a single run.

The stress of the deposited AlN films changes from 0.9 GPa (tensile) to -4 GPa (compressive), with increasing ion flux density, but was found to be independent on the sample temperature between 100 °C and 500 °C. All films showed a (001)-texture with columnar grains. The observed evolution from an open to a closed grain boundary morphology with increasing ion flux is compatible with the observed stress evolution. From this we conclude that a well-designed magnetic field generated by a coil is an experimental parameter that allows a precise control of the film properties in a confocal magnetron sputtering system.

Acknowledgments

Support from the Swiss National Science Foundation (project Nr. 200021_150095), and Empa is hereby gratefully acknowledged. We thank S.M. Vranjkovic for designing the in-situ coil and the Langmuir probe holder, and for his help in installing these systems in our sputter deposition chamber.

We thank Max Döbeli from the Laboratory for Ion Beam Physics of ETHZ for the ERDA and RBS measurements and analysis, as well as Erwin Hack from the Laboratory for Transport at Nanoscale Interfaces at Empa for the ellipsometry measurements and the helpful discussions.

References

[1] A. Anders, A structure zone diagram including plasma-based deposition and ion etching, Thin Solid Films 518 (15) (2010) 4087–4090, http://dx.doi.org/10.1016/j.tsf.2009.10.145.
[2] A. Anders, Handbook of Plasma Immersion Ion Implantation and Deposition, Wiley, 2000.
[3] T. Itoh, Ion Beam Assisted Film Growth, Elsevier B.V., 1989.
[4] M. Nastasi, M. Wolfhard, W. Ensinger, Ion implantation and thin-film deposition, in: A. Anders (Ed.) Handb. Plasma Immers. Ion Implant. Depos., in: Wiley, 2000, pp. 125–242.
[5] I. Petrov, F. Adibi, J.E. Greene, L. Hultman, J.-E. Sundgren, Average energy deposited per atom: a universal parameter for describing ionassisted film growth? Appl. Phys. Lett. 63 (1) (1993) 36–38, http://dx.doi.org/10.1063/1.109742.
[6] I. Petrov, L. Hultman, U. Helmersson, J.-E. Sundgren, J. Greene, Microstructure modification of TiN by ion bombardment during reactive sputter deposition, Thin Solid Films 169 (2) (1989) 299–314, http://dx.doi.org/10.1016/0040-6090(89)90713-X.
[7] O. Baranov, K. Bazaka, H. Kersten, M. Keidar, U. Cvelbar, S. Xu, I. Levchenko, Plasma under control: advanced solutions and perspectives for plasma flux

management in material treatment and nanosynthesis, Appl. Phys. Rev. 4 (4) (2017) 041302, http://dx.doi.org/10.1063/1.5007869.
[8] I. Petrov, F. Adibi, J.E. Greene, W.D. Sproul, W. Münz, Use of an externally applied axial magnetic field to control ion/neutral flux ratios incident at the substrate during magnetron sputter deposition, J. Vac. Sci. Technol. A Vacuum, Surfaces, Film. 10 (5) (1992) 3283–3287, http://dx.doi.org/10.1116/1.577812.
[9] C. Engström, T. Berlind, J. Birch, L. Hultman, I. Ivanov, S. Kirkpatrick, S. Rohde, Design, plasma studies, and ion assisted thin film growth in an unbalanced dual target magnetron sputtering system with a solenoid coil, Vacuum 56 (2) (2000) 107–113, http://dx.doi.org/10.1016/S0042-207X(99)00177-3.
[10] J. Musil, Flexible hard nanocomposite coatings, RSC Adv. 5 (74) (2015) 60482–60495, http://dx.doi.org/10.1039/C5RA09586G.
[11] E. Lewin, D. Loch, A. Montagne, A.P. Ehiasarian, J. Patscheider, Comparison of AlSiN nanocomposite coatings deposited by HIPIMS and DC magnetron sputtering, Surf. Coatings Technol. 232 (2013) 680–689, http://dx.doi.org/10.1016/j.surfcoat.2013.06.076.
[12] M. Akiyama, T. Kamohara, K. Kano, A. Teshigahara, Y. Takeuchi, N. Kawahara, Enhancement of piezoelectric response in scandium aluminum nitride alloy thin films prepared by dual reactive cosputtering, Adv. Mater. 21 (5) (2009) 593–596, http://dx.doi.org/10.1002/adma.200802611.
[13] M.-A. Dubois, P. Muralt, Properties of aluminum nitride thin films for piezoelectric transducers and microwave filter applications, Appl. Phys. Lett. 74 (20) (1999) 3032–3034, http://dx.doi.org/10.1063/1.124055.
[14] R. Elfrink, T.M. Kamel, M. Goedbloed, S. Matova, D. Hohlfeld, Y. van Andel, R. van Schaijk, Vibration energy harvesting with aluminum nitride-based piezoelectric devices, J. Micromech. Microeng. 19 (9) (2009) 094005, http://dx.doi.org/10.1088/0960-1317/19/9/094005.
[15] J. Bjurström, V. Yantchev, M. Moreira, I. Katardjiev, Efficient RF voltage transformer with bandpass filter characteristics, Electron. Lett. 49 (3) (2013) 198–199, http://dx.doi.org/10.1049/el.2012.3982.
[16] M. a. Moreira, T. Törndahl, I. Katardjiev, T. Kubart, Deposition of highly textured AlN thin films by reactive high power impulse magnetron sputtering, J. Vac. Sci. Technol. A Vacuum, Surfaces, Film. 33 (2) (2015) 021518, http://dx.doi.org/10.1116/1.4907874.
[17] M.-A. Dubois, P. Muralt, Stress and piezoelectric properties of aluminum nitride thin films deposited onto metal electrodes by pulsed direct current reactive sputtering, J. Appl. Phys. 89 (11) (2001) 6389–6395, http://dx.doi.org/10.1063/1.1359162.
[18] S. Fichtner, T. Reimer, S. Chemnitz, F. Lofink, B. Wagner, Stress controlled pulsed direct current co-sputtered Al 1 × Sc × N as piezoelectric phase for micro-mechanical sensor applications, APL Mater. 3 (11) (2015) 116102, http://dx.doi.org/10.1063/1.4934756.
[19] B. Window, N. Savvides, Charged particle fluxes from planar magnetron sputtering sources, J. Vac. Sci. Technol. A Vacuum, Surfaces, Film. 4 (2) (1986) 196–202, http://dx.doi.org/10.1116/1.573470.
[20] R. Wiese, H. Kersten, G. Wiese, R. Bartsch, Energy influx measurements with an active thermal probe in plasma-technological processes, EPJ Tech. Instrum. 2 (1) (2015) 2, http://dx.doi.org/10.1140/epjti/s40485-015-0013-y.
[21] M. Ohring, Materials Science of Thin Films, Elsevier Science, 2001.
[22] D.A. Jaeger, Interface Investigations on Titanium Nitride Bilayer Systems, Ph.D. thesis (2012) http://infoscience.epfl.ch/record/181534http://dx.doi.org/10.5075/epfl-thesis-5509.
[23] A. Piel, Plasma Physics, vol. 1, Springer Berlin Heidelberg, Berlin, Heidelberg, 2010, pp. 1689–1699, http://dx.doi.org/10.1007/978-3-642-10491-6.
[24] K.M. Pollock, T. Kaufman-Osborn, J. Hiltrop, J.R. Doyle, Effects of temperature and near-substrate plasma density on the structural and electrical properties of DC sputtered germanium thin films, J. Vac. Sci. Technol. A Vacuum, Surfaces, Film. 29 (5) (2011) 051301, http://dx.doi.org/10.1116/1.3607410.
[25] H. Kersten, H. Deutsch, H. Steffen, G. Kroesen, R. Hippler, The energy balance at substrate surfaces during plasma processing, Vacuum 63 (3) (2001) 385–431, http://dx.doi.org/10.1016/S0042-207X(01)00350-5.
[26] G. Este, W.D. Westwood, Stress control in reactively sputtered AlN and TiN films, J. Vac. Sci. Technol. A Vacuum, Surfaces, Film. 5 (4) (1987) 1892–1897, http://dx.doi.org/10.1116/1.574480.
[27] F. Medjani, R. Sanjinés, G. Allidi, A. Karimi, Effect of substrate temperature and bias voltage on the crystallite orientation in RF magnetron sputtered AlN thin films, Thin Solid Films 515 (1) (2006) 260–265, http://dx.doi.org/10.1016/j.tsf.2005.12.145.
[28] J. Lin, R. Chistyakov, C-axis orientated AlN films deposited using deep oscillation magnetron sputtering, Appl. Surf. Sci. 396 (2017) 129–137, http://dx.doi.org/10.1016/j.apsusc.2016.11.025.
[29] A. Pelisson, M. Parlinska-Wojtan, H. Hug, J. Patscheider, Microstructure and mechanical properties of AlSiN transparent hard coatings deposited by magnetron sputtering, Surf. Coatings Technol. 202 (4-7) (2007) 884–889, http://dx.doi.org/10.1016/j.surfcoat.2007.05.094.
[30] C. Duquenne, P.Y. Tessier, M.P. Besland, B. Angleraud, P.Y. Jouan, R. Aubry, S. Delage, M.A. Djouadi, Impact of magnetron configuration on plasma and film properties of sputtered aluminum nitride thin films, J. Appl. Phys. 104 (6) (2008) 063301, http://dx.doi.org/10.1063/1.2978226.
[31] M. Ishihara, S. Li, H. Yumoto, K. Akashi, Y. Ide, Control of preferential orientation of AlN films prepared by the reactive sputtering method, Thin Solid Films 316 (1-2) (1998) 152–157, http://dx.doi.org/10.1016/S0040-6090(98)00406-4.
[32] A. Pelisson, Al-Si-N Transparent Hard Nanostructured Coatings, Ph.D. thesis University of Basel, 2009, https://edoc.unibas.ch/1000/1/Dissertation-Pelisson{_}Volltext{_}Unibas09.pdf.
[33] H. Schulz, K.H. Thiemann, Crystal structure refinement of AlN and GaN, Solid State Commun. 23 (11) (1977) 815–819, http://dx.doi.org/10.1016/0038-1098(77)90959-0.
[34] D.M. Többens, N. Stüßer, K. Knorr, H.M. Mayer, G. Lampert, E9: the new high-resolution neutron powder diffractometer at the Berlin neutron scattering center, Mater. Sci. Forum, vol. 378, Trans Tech Publ, 2001, pp. 288–293.